

1 **Investigation of the functional relationship between antecedent rainfall and the probability**
2 **of debris flow occurrence in Jiangjia Gully, China**

3 Shaojie Zhang¹, Xiaohu Lei^{1,4}, Hongjuan Yang¹, Kaiheng Hu¹, Juan Ma², Dunlong Liu³, Fanqiang Wei⁴

4 1. State Key Laboratory of Mountain Hazards and Engineering Safety, Institute of Mountain Hazards and
5 Environment, Chinese Academy of Sciences, Chengdu 610041, China

6 2. China Institute for Geo-Environment Monitoring, Beijing, 100081

7 3. College of Software Engineering, Chengdu University of Information and Technology, Chengdu, 610225, China

8 4. Chongqing Institute of Green and Intelligent Technology, Chinese Academy of Sciences, Chongqing 400714,
9 China

10 Correspondence to: Shaojie Zhang, E-mail: sj-zhang@imde.ac.cn; Kaiheng Hu, E-mail: khhu@imde.ac.cn

11 **Abstract**

12 A larger antecedent effective precipitation (AEP) indicates a higher probability of a debris flow
13 (P_{df}) being triggered by subsequent rainfall. Scientific topics surrounding this qualitative conclusion
14 that can be raised, including what kinds of variation rules do they follow, and whether there is a
15 boundary limit. To answer these questions, Jiangjia Gully in Dongchuan, Yunnan province, China,
16 is chosen as the study area, and a numerical calculation, rainfall scenario simulation, and Monte
17 Carlo integration method have been used to calculate the occurrence probability of debris flow under
18 different AEP conditions and derive the functional relationship between P_{df} and AEP. The
19 relationship between P_{df} and AEP can be quantified by a piecewise function. P_{df} is equal to 15.88%
20 even AEP reaches 85 mm indicating that debris flow in nature has an extremely small probability
21 compared to the rainfall frequency. Data from 1094 rainfall events and 37 historical debris flow

22 events are collected to verify the reasonability of the functional relationship. The results indicate
23 that the piecewise function are highly correlated with the observation results. Our study confirms
24 the correctness of the qualitative description of the relationship between AEP and P_{df} , clarifies that
25 debris flow is a small probability event compared to rainfall frequency, and quantitatively reveals
26 the evolution law of debris flow occurrence probability with AEP, which can provide a clear
27 reference for the early warning of debris flows.

28 **Keywords:** Debris flow, antecedent effective rainfall, Dens-ID, Monte Carlo method

29

30 **1 Introductions**

31 The antecedent effective precipitation (AEP) likes a Trojan horse lurking inside a loose soil
32 mass, which can cooperate with subsequent rainfall at any time to trigger debris flow in a debris-
33 flow gully. The AEP is equivalent to the precipitation preserved in soil mass before the triggering
34 rainfall process; it represents the saturation degree of loose soil mass (Segoni et al., 2018a;
35 Leonarduzz and Molnar, 2020). Therefore, the soil moisture that has accumulated from antecedent
36 rainfall since the beginning of a rainfall season has a significant influence on how new storm rainfall
37 interacts with the loose soil mass within a gully (Fiorillo and Wilson, 2004; Long et al., 2020). The
38 increase in AEP can decrease the shear strength of a loose solid material provided by shallow
39 landslides or channel erosion (Papa, et al., 2013; Senthilkumar et al., 2017; Liu et al., 2020), as a
40 consequence, the supply rate of solid material resources can be significantly enhanced in the
41 subsequent rainfall process (Wei et al., 2008; Bennett et al., 2014; Zhang et al., 2020). Additionally,
42 increased AEP and moisture content have been shown to enhance rainfall-induced surface runoff in
43 a variety of environments (Tisdall, 1951; Luk, 1985; Le Bissonnais et al., 1995; Castillo et al., 2003;

44 Jones et al., 2017; Hirschberg et al., 2021). Thus, AEP plays an important role in the formation of
45 debris flows (Hong et al., 2018).

46 Rainfall thresholds represent the difficulty degree of debris flow triggered by rainfall (Marra
47 et al., 2017). Investigations including the influence of AEP on the rainfall threshold can be helpful
48 to examining the relationship between AEP and debris flow occurrence. Currently, the relationship
49 between the AEP and rainfall threshold indicates that there is a negative correlation between the
50 AEP and rainfall conditions that trigger debris flows (Huang, 2013). AEP also represents the
51 saturation degree of loose soil mass (Zhao et al., 2019a; Abraham et al., 2021), and integrating soil
52 moisture with rainfall thresholds has been proven effective in improving prediction performance
53 (Segoni et al., 2018a; Zhao et al., 2019b; Abraham et al., 2020). Scholars also have attempted to
54 analyze the influence of antecedent soil moisture on the rainfall threshold triggering debris flow
55 (Cui et al., 2007; Hu et al., 2015), and there is still a negative correlation between antecedent soil
56 moisture and triggering rainfall conditions (Chen et al., 2017) just like the relationship between AEP
57 and rainfall threshold. The above investigations show that increasing in AEP can significantly
58 decrease the rainfall conditions for triggering a debris flow, which in turn means that debris flow is
59 more likely to occur. Generally, the qualitative description of ‘the greater the AEP, the higher the
60 probability (P_{df}) of subsequent rainfall triggering the debris flow (De Vita et al., 2000; Bel et al.,
61 2017)’ has gradually become a consensus. Therefore, discovering a specific function to describe this
62 qualitative description is helpful to further demonstrating the above consensus, revealing a certain
63 evolutionary law of debris flow with rainfall in nature.

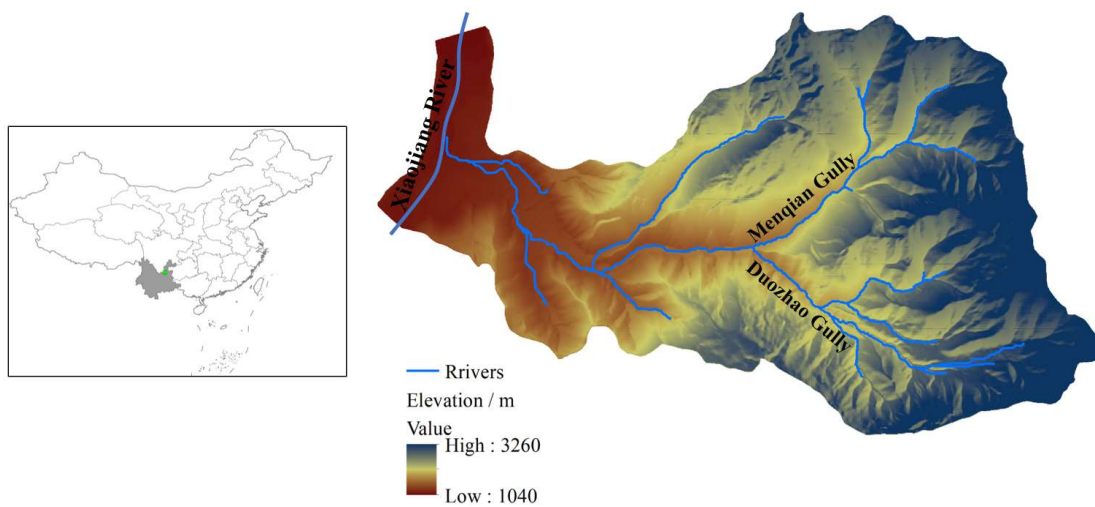
64 To quantify the evolution law of P_{df} with the changing AEP, a numerical model denoted as the
65 Dens-ID can correlate the rainfall parameters (I and D) with the debris flow density (Zhang et al.,

2020; Long et al., 2020; Zhang et al., 2023), and it has been used to construct the rainfall intensity-duration (ID) threshold curves under different AEP conditions. The ID threshold curves with upper and lower bounds can delineate the closed region in the ID coordinate system, which represents the set of all rainfall conditions that can trigger debris flow at a certain AEP. Consequently, the probability of natural rainfall falling into a closed region is equivalent to P_{df} , which can then be calculated based on Monte Carlo integration. The next section introduces the basic information of study area including the rainfall and debris flow event data collected from the study area. The third section addresses how to establish the functional relationship between the AEP and Pdf using the Dens-ID and Monte Carlo integration method. Section 4, 5 and 6 discuss the results and state the conclusions of this study, respectively.

2 Study areas

The Jiangjia Gully (JJG) is a primary tributary of the Xiaojiang River, which is located in the Dongchuan District of Kunming City, Yunnan Province, China (Fig.1). As shown in Fig.1, JJG has a drainage area of 48.6 km² with elevations ranging from 1040 to 3260 m. In this gully, the relative relief from the ridge to the valley reaches 500 m, and most of the slope gradient is greater than 25°. Slopes within JJG are covered by abundant loose soil with a thickness of more than ten meters. Shallow landslides are frequently triggered by intense rainfall processes in JJG, providing a large number of solid materials for debris flow (Yang et al., 2022). Before 1979, the Menqian and Duozhao gullies are the two main tributaries of JJG, accounting for 64.7% of the entire drainage area. The upstream areas of the two main tributaries are the initiation zones of the debris flows, and the channels of the upstream tributaries are narrow and V-shaped (Zhang et al., 2020). However, several check dams have been constructed in the Duozhao gully since 1979, which have significantly reduced debris flow activity in this sub-gully (Zeng et al., 2009). Currently, Menqian Gully with the area of 13.2 km² is the primary source area. The slope gradient of its both sides is very steep, e.g., the mean slope in Menqian Gully is 32° and the maximum slope can reach 70°.

91 Bedrock that mainly consists of slates formed in lower Proterozoic crops out in the unvegetated or
92 sparsely vegetated lower part. The bedrock is fragmented and mostly disintegrates into clasts with
93 the size more than 20 mm. The upper part of the bedrock is lain by soil mantles with thicknesses of
94 0.5–20 m, which are covered by grasses and shrubs, or are used for terrace farming. The soil mantle
95 is poorly sorted and composed of particles from clay to boulder. The translational zone from the
96 upper to the lower parts of the slope is prone to shallow landslides. Some landslides directly evolve
97 into debris flows, while the others release sediment to the channel, which is mobilized by runoff in
98 debris flow events (Yang et al., 2022).



99

100 Fig.1 Location of JJG

101 Steep terrain provides a beneficial potential energy condition for transporting a large amount
102 of loose solid materials from JJG to Xiaojiang River. Consequently, debris flows in JJG can be easily
103 triggered by high-intensity rainstorm or long-duration rainfall processes (Zhang et al., 2020). The
104 solid material necessary for a debris flow in a gully may be from shallow landslides (Iverson et al.,
105 1997; Gabet and Mudd, 2006; Zhang et al., 2020; Long et al., 2020) or runoff-induced bed erosions
106 (Berti and Simoni, 2005; Coe et al., 2008; Tang et al., 2020; Bernard and Gregoretti, 2021). In JJG,
107 shallow landslides are the main sources for the solid material supply (Zhang et al., 2014; Liu et al.,
108 2016; Yang et al., 2022), which is consistent with the assumptions of Dens-ID (Zhang et al., 2020).
109 Thus, JJG is used as the study zone for deriving the function that describes the relationship between

110 AEP and P_{df} .

111 **3 Methods and data**

112 **3.1 Dens-ID**

113 Debris flow gullies characterized by a solid source supply from landslides are widely
114 distributed in southwest China (Zhang et al., 2014). For this type of debris flow gully, our previous
115 study proposed Dens-ID aiming at correlating debris-flow density to rainfall parameters based on
116 water-soil coupling mechanism (Zhang et al., 2020; Long et al., 2020). Den-ID assumes debris flow
117 to be a water-soil mixture, it contains three core simulating contents including hydrological
118 simulation, water-soil coupling to calculate the water-soil-mixture density, and correlating density
119 to rainfall parameters.

120 (1) Simulating hydrological process: the purpose is to provide parameters for estimating
121 rainfall-induced runoff and the supply volume of rainfall-induced loose solid materials. Based on
122 the digital elevation model (DEM) of a gully, Den-ID can simulate the rainfall-induced runoff and
123 water diffusion in the vertical direction within the soil mass. The rainfall infiltration border is
124 controlled by [Eq. Equation 1](#).

$$125 \quad -D(\theta) \frac{\partial \theta}{\partial z} + K(\theta) = I(t) \quad (1)$$

126 where θ is the soil water content; $D(\theta) = K(\theta)/(d\theta/d\psi)$, which represents the soil water
127 diffusivity; z is the soil depth, which is positive downwards along the soil depth as the topsoil is
128 taken as the origin point; $K(\theta)$ is the hydraulic conductivity; $I(t)$ is the rainfall intensity; and ψ is
129 the soil matrix suction. When the rainfall intensity is less than the surface infiltration capacity,
130 [Eq. Equation 1](#) is used to represent this physical process; whereas the case of precipitation intensity
131 exceeding the infiltration capacity of topsoil means that the surface is saturated, and the excess

132 precipitation from the topsoil is converted into runoff. Therefore, the pressure infiltration of each
 133 grid cell is not considered.

$$134 \quad \frac{\partial \theta}{\partial t} = \frac{\partial}{\partial z} [D(\theta) \frac{\partial \theta}{\partial z}] - \frac{\partial K(\theta)}{\partial z} \quad (2)$$

135 [Eq.Equation 2](#) is the Richard differential infiltration equation (Richards, 1931), which is used to
 136 describe the water movement along the vertical direction within soil mass after precipitation
 137 infiltrates into topsoil. Dens-ID uses the finite-difference method to solve Eqs. 1 and 2 and can
 138 provide the runoff depth (denoted as $dw(i, t)$), soil water content, and soil matrix suction for each
 139 grid cell. Dens-ID then calculates the runoff volume using runoff depth $dw(i, t)$ in [Eq.Equation 3](#).

$$140 \quad V_w(t) = \sum_{t=1}^T \sum_{i=1}^n S_g * dw(i, t) \quad (3)$$

141 where n represents the total number of grid cells that can generate runoff at time t , $V_w(t)$ represents
 142 the total volume of runoff within a gully at time t , S_g represents the area of the grid cell generating
 143 runoff, and T represents the total duration of a rainfall process.

144 (2) Calculating supply amount of loose solid materials and density of the water-soil mixture:
 145 taking hydrological parameters such as soil water content and soil matrix suction as inputs, Dens-
 146 ID uses [Eqs.Equations 4 and 5](#) to estimate the supply amount of rainfall-induced loose solid
 147 materials within a gully. [Eq.Equation 4](#) calculates safety factor F_s of each grid cell as a function of
 148 the matrix suction and soil moisture. $F_s > 1$ indicates that the grid cell is stable and cannot supply
 149 solid material to the gully, whereas a grid with $F_s < 1$ can provide solid material in the form of a
 150 shallow landslide.

$$151 \quad F_s = \frac{\tan \varphi}{\tan \beta} + \frac{c + \psi \tan(\varphi^b)}{\gamma_t d_s \cos \beta \sin \beta} \quad (4)$$

152 where F_s represents the safety factor of each grid cell, c is the soil cohesion force, φ is the internal
 153 friction angle, φ^b is related to the matrix suction and is approximately equal to φ as the low matrix

154 suction is small, d_s is the soil depth, and ψ is the matrix suction which is a function of soil water
 155 content and can be described by the Van Genuchten model (Van Genuchten, 1980).

156 ~~Using d_s derived from Eq. 3 as input, Eq. Equation~~ 4 is used to estimate the total volume of
 157 solid materials from all the ~~instable-unstable~~ grid cells during a rainfall process.

$$158 \quad V_s(t) = \sum_{t=1}^T \sum_{j=1}^m S_g * ds(j, t) \quad (5)$$

159 where m represents the number of grid cells that can provide solid material at time t and $V_s(t)$ is the
 160 total volume of solid material within a gully at time t . At time t , the density of the water-soil mixture
 161 after full coupling between runoff and solid material can be calculated using Eq. Equation 6.

$$162 \quad \rho_{mix}(t) = \frac{\rho_w V_w(t) + \rho_s V_s(t)}{V_{mix}(t)} \quad (6)$$

163 where $\rho_{mix}(t)$ is the density of the water-soil mixture, ρ_w is the water density, ρ_s is the density of
 164 the soil particles, and $V_{mix}(t)$ is the volume of the water-soil mixture, which is the sum of $V_w(t)$
 165 and $V_s(t)$. $V_w(t)$ and $V_s(t)$ are the key variables that can be derived using Eqs. 3 and 5.

166 (3) Correlating density to rainfall parameters including rainfall intensity and ~~duration: Dens-~~
 167 ~~ID~~ ~~duration: after~~ firstly ~~preset~~ ~~presettings~~ the density of the water-soil mixture as ρ_{mix} , ~~it~~ ~~Dens-ID~~
 168 ~~also~~ needs to simulate many rainfall scenarios including long durations with low-intensity rainfall
 169 and short durations with high-intensity rainfall in order to obtain a sufficient number of $[D_i, I_i]$.
 170 Using each $[D_i, I_i]$ as input, Dens-ID then can calculate the density using Eq. Equation 6. If the
 171 calculated density is equal to ρ_{mix} , the $[D_i, I_i]$ combination is saved by Dens-ID. After Dens-ID
 172 completes the trial calculations, all combination data of $[D_i, I_i]$ that satisfy the constraints of the
 173 preset density (ρ_{mix}) can be collected as a dataset. Each collected $[D_i, I_i]$ within the dataset
 174 corresponds to the preset ρ_{mix} , accordingly, Dens-ID can correlate rainfall parameters (D and I) to
 175 debris flow density (Long et al., 2020). Dens-ID can derive ID threshold curves by fitting the

176 selected $[D_i, I_i]$ data, and each ID curve corresponds to a debris flow density value (Zhang et al.,
177 2020). As the density of debris flow in JJG varies in a specific interval of $1.2\text{--}2.3\text{g/cm}^3$ (Zhang et
178 al., 2014; Zhuang et al., 2015; Long et al., 2020), the threshold curve that corresponds to the
179 boundary value can form a closed area with the I- and D-axes in the ID coordinate system. The case
180 of monitoring or forecasting rainfall falling into this closed area indicates that the rainfall condition
181 may trigger debris flow. The verification results in JJG show that Dens-ID can effectively describe
182 the mechanism and process of debris flow formation, and its prediction accuracy is approximately
183 80.5%, which is 27.7% higher than that of statistical models (Zhang et al., 2020). Such a high
184 prediction accuracy can further indicate that the closed area formed by the derived ID curves has a
185 very reasonable location and coverage in the ID coordinate system, providing extremely reliable
186 analytical data in this study.

187 **3.2 JJG data for model Dens-ID**

188 The JJG datasets for Dens-ID are terrain data, hydrological parameters, and soil mechanical
189 parameters. The DEM is the basal data for deriving other terrain data, including slope length,
190 gradient, and river channels; the spatial resolution of the DEM is 0.5 m, and a DEM with a grid size
191 of 10 m was generated using the resampling technology in ArcGIS. The hydrological parameters
192 are related to the soil types within JJG; the five key parameters are the saturated soil water content,
193 residual soil water content, the two parameters of soil water characteristic curve including n and m ,
194 and the infiltration rate of topsoil. The soil mechanical parameters are the soil cohesion force and
195 internal friction angle obtained through direct shear tests on the soil samples. Detailed data are
196 available in Zhang et al. (2020) and Long et al. (2020).

197 3.3 Historical rainfall and debris flow data

198 Rainfall data for the rainy seasons between 2006 and 2020 have been collected from the JJG
199 observation station, and it is necessary to identify each rainfall process from the long-term rainfall
200 sequences. Inter-event time (IET) is defined as the minimum time interval between two consecutive
201 rainfall pulses (Adams et al., 1986). IET has a strong influence on the rainfall event starting and
202 ending times (Bel et al., 2017), and Peres et al. (2018) has identified that IET depends on whether
203 the mean daily potential evapotranspiration (MDPE) is larger than precipitation within the IET. The
204 long observation of evaporation within JJG showed that MDPE is about 4 mm; precipitation during
205 IET >0.5 mm is considered the end of a rainfall process. Under this standard, 1094 rainfall events
206 and 37 debris flow events have been identified during the sampling period. Detailed rainfall data
207 information can be found in “appendix 1-1094 rainfall and 37 debris flow data.xlsx”. The AEP listed
208 in this appendix is considered the weighted sum of the rainfall periods before the occurrence of
209 debris flow (Long et al., 2020) and it can be calculated using [Eq-Equation 7](#).

$$210 \quad AEP = \sum_{i=1}^n K^n R_i \quad (7)$$

211 where AEP is the antecedent effective rainfall; K is the attenuation coefficient, which is equal to
212 0.78 based on the field test in JJG (Zhang et al., 2020); and n is the number of days preceding the
213 debris flow occurrence.

214 Based on the observed rainfall data, the 1094 AEPs are calculated using [Eq-Equation 7](#) and
215 listed in Appendix 1. The AEP corresponding to each rainfall event varies from 0–88 mm. Taking
216 this variation range as a reference, the variation range of the AEP input in the Dens-ID model is set
217 between 10 and 85 mm. [Since AEP in JJG ranges in 0-88 mm according to the measured rainfall](#)
218 [data](#). Dens-ID presets several AEP values including 10, 15, 20, 25, 30, 35, 40, 45, 50, 55, 60, 65, 70,

219 75, 80, 85. The cases of AEP=0 and AEP=5 mm are excluded, because the two cases represents such
 220 a low initial rainfall condition that any ID curve cannot derived from Dens-ID. The purpose of
 221 increasing AEP by an interval of size 5 is to get adequate ID curves, which will be helpful to
 222 calculate P_{df} can be calculated under different AEP conditions.

223 3.4 Monte Carlo method for calculating the definite integral

224 Because of the boundary of the debris-flow density in JJG (1.2–2.3g/cm³), Dens-ID produces
 225 the corresponding upper and lower boundary curves under a specific AEP condition. The two
 226 boundary curves can be described using the power function.

$$227 \begin{cases} f(D)_{up} = I_{up} = \alpha_1 D^{\beta_1} & D \in [a_1, b_1] \\ f(D)_{low} = I_{low} = \alpha_2 D^{\beta_2} & D \in [a_2, b_2] \end{cases} \quad (8)$$

228 These two threshold curves can delineate an enclosed area in the ID coordinate system, denoted
 229 as W_{ID} . The independent variable (D) and dependent variable (I) in [Eq. Equation 8](#) also form a closed
 230 rectangular region in the ID coordinate system, denoted as R_{ID} . In the ID coordinate system, the
 231 coverage of R_{ID} is larger than that of W_{ID} , as will be shown in detail in Section 4.1. Limited within
 232 R_{ID} , any rainfall processes located in W_{ID} can trigger debris flow. If the probability of rainfall
 233 process falling into the range of W_{ID} under random conditions is determined, the occurrence
 234 probability of debris flow can be estimated. Many physical phenomena are stochastic in nature and
 235 governed by stochastic partial differential equations with nondeterministic initial/boundary
 236 conditions or integral equations (Peres and Cancelliere, 2014; Yan and Hong, 2014). Albert (1956)
 237 proposed the Monte Carlo method for solving integral equations. This method is subsequently used
 238 to estimate the peak flow and volume of debris flow (Donovan and Santi, 2017; Paola et al., 2017),
 239 entrainment of the underlying bed sediment (Han et al., 2015), and risk assessment (Calvo and Savi,

240 2009; Li et al., 2021). The rainfall process is randomly selected within the R_{ID} , and the probability
 241 of the chosen one falling into the W_{ID} can be determined using W_{ID}/R_{ID} . The physical meaning of
 242 the Monte Carlo solving definite integral lies on calculating the area enclosed by the function curve
 243 and horizontal axis. Therefore, the area of W_{ID} can be calculated by the difference in the definite
 244 integral formula of the two equations in [Eq. Equation 8](#).

$$245 \quad W_{ID} = S_{up} - S_{low} = \int_{a_1}^{b_1} f(D)_{up} dD - \int_{a_2}^{b_2} f(D)_{low} dD \quad (9)$$

246 where S_{up} and S_{low} represent the area enclosed by the two threshold curves and the horizontal axis,
 247 respectively, and a_1 , b_1 , a_2 , and b_2 are the boundary values of D in the two curves. For the upper
 248 boundary line (or lower boundary), if the probability distribution function of D between $[a_1, b_1]$ is

249 $p(D)$, [Eq. Equation 10](#) can be derived by substituting $p(D)$ into [Eq. Equation 9](#).

$$250 \quad \begin{cases} S_{up} = \int_{a_1}^{b_1} f(D)_{up} dD = \int_{a_1}^{b_1} \frac{f(D)_{up}}{p(D)} p(D) dD \approx \frac{1}{n} \sum_{k=1}^n \frac{f(D_i)_{up}}{p(D_i)} \\ S_{low} = \int_{a_2}^{b_2} f(D)_{low} dD = \int_{a_2}^{b_2} \frac{f(D)_{low}}{p(D)} p(D) dD \approx \frac{1}{n} \sum_{k=1}^n \frac{f(D_i)_{low}}{p(D_i)} \end{cases} \quad (10)$$

$$251 \quad W_{ID} = \frac{1}{n} \sum_{k=1}^n \frac{f(D_i)_{up}}{p(D_i)} - \frac{1}{n} \sum_{k=1}^n \frac{f(D_i)_{low}}{p(D_i)} \quad (11)$$

252 where n represents the number of random samples drawn from the variation range of D , and $p(D_i)$
 253 is the probability density distribution function of D in the interval $[a_1, b_1]$ or $[a_2, b_2]$. The key to
 254 solving [Eq. Equation 10](#) depends on sampling from $p(D)$. The following steps are used to explain
 255 how samples were taken using $p(D_i)$.

256 Step 1: Based on the probability density distribution function $p(D)$, the cumulative probability
 257 distribution function can be derived by $cdf(D) = \int_{-\infty}^D f(D) dD$;

258 Step 2: Assume that $U^{(i)}$ obeys a uniform distribution within $[0, 1]$, which can be randomly collected
 259 from this interval and denoted as $U^{(i)} \sim U(0, 1)$.

260 Step 3: Substitute $U^{(i)}$ into the inverse function of the cumulative probability distribution $cdf(D)$ to
 261 obtain random sample $D^{(i)}$, denoted by $D^{(i)} = cdf^{-1}(U^{(i)})$. Then, a dataset composed of n data

262 points of $D^{(i)}$ is obtained.

263 Step 4: W_{ID} can be calculated by substituting n data points of $D^{(i)}$ into [Eq. Equation 10](#), and the P_{df}
264 ($P_{df} = \frac{R_{ID}}{W_{ID}}$) corresponding to a specific AEP is determined. P_{df} represents the probability that the
265 subsequent precipitation process may trigger debris flow for a certain AEP. Thus, the influence of
266 the AEP on the occurrence probability of debris flows can be quantified.

267 3.5 Correlation analysis between numerical and observation results

268 The relationship between the AEP- P_{df} fitted through the observational data is used as a
269 reference standard, and the correlation analysis method is used to verify the function of the AEP- P_{df}
270 derived by Dens-ID. Correlation analysis is used to study the degree of linear correlation between
271 variables, which is represented by correlation coefficient r :

$$272 \quad r = \frac{\sum_{i=1}^n (x_i - \bar{x})(y_i - \bar{y})}{\sqrt{\sum_{i=1}^n (x_i - \bar{x})^2 \sum_{i=1}^n (y_i - \bar{y})^2}} \quad (12)$$

273 where x represents the P_{df} derived from the observed data, y represents the P_{df} derived from Dens-
274 ID, \bar{x} and \bar{y} represent the averages, r represents the correlation coefficient, and n represents the
275 number of samples. $|r| \geq 0.8$ can be regarded as a high correlation between two variables; $0.5 \leq |r| < 0.8$
276 represents a moderate correlation; $0.3 \leq |r| < 0.5$ represents a low correlation; and $|r| < 0.3$ indicates the
277 degree of correlation between the two variables is weak and can be regarded as uncorrelated.

278 4 Results

279 4.1 ID threshold curves and warning zone closed by the derived curves

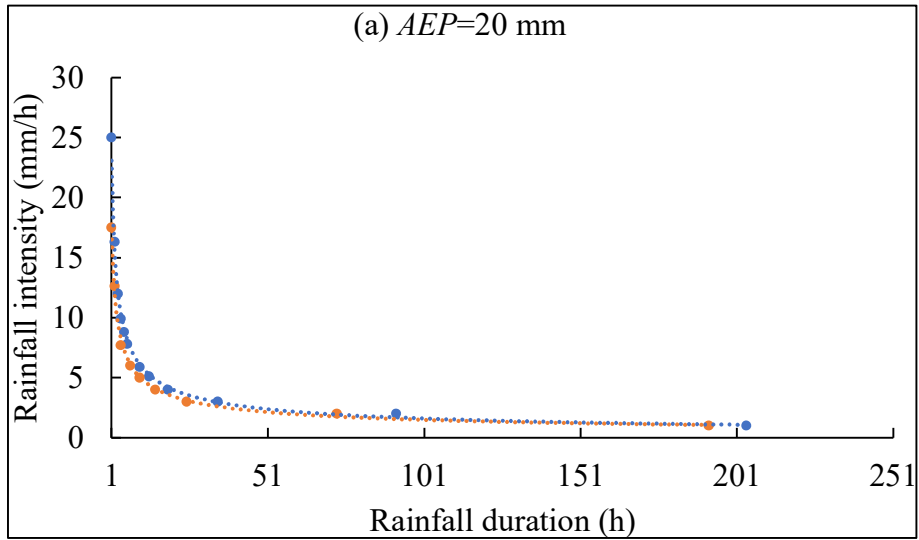
280 Dens-ID yields the upper and lower boundary lines of the ID threshold in each condition of a
281 preset AEP, and these two boundary lines are characterized by different debris flow density and
282 listed in Table 1. It can be seen from Table 1 that the maximum density corresponding to the ID
283 threshold curve cannot reach 2.2, when AEP is less than 15 mm. A small AEP indicates the supply

284 rate of solid resources in JJG is far less than the runoff generation rate during a subsequent rainfall
 285 process. In this situation, runoff is dominated in the water-soil coupling process yielding a water-
 286 soil mixture with low density value.

287 Table 1 ID threshold curve database under different AEP

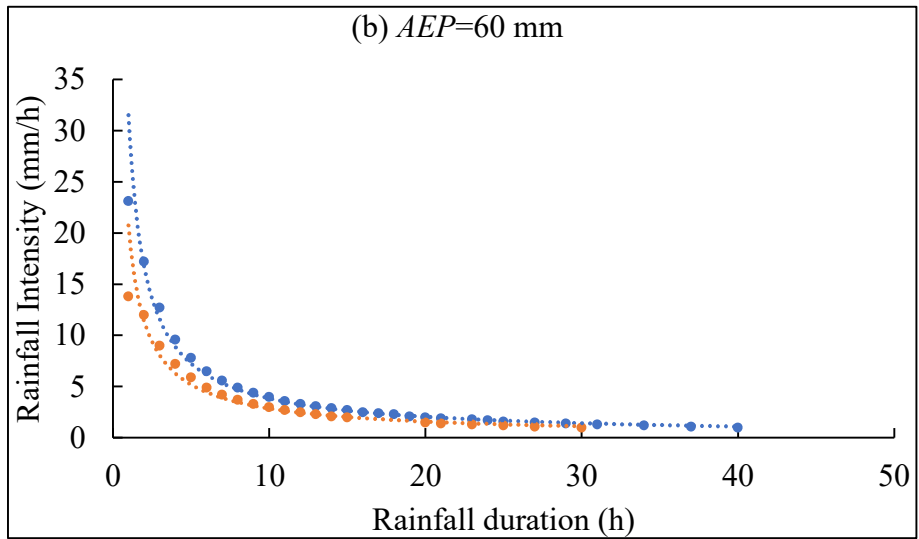
AEP (mm)	ID threshold curve function for JJG	
	1.2 g/cm ³	2.2 g/cm ³
10	$I_{1.2} = 19.85D^{-0.54} D \in [1, 269] (R^2 = 0.991)$	$I_{1.8} = 15.85D^{-0.48} D \in [1, 263] (R^2 = 0.990)$
15	$I_{1.2} = 21.69D^{-0.55} D \in [1, 236] (R^2 = 0.993)$	$I_{2.0} = 16.10D^{-0.50} D \in [1, 229] (R^2 = 0.995)$
20	$I_{1.2} = 23.22D^{-0.58} D \in [1, 203] (R^2 = 0.996)$	$I_{2.2} = 17.20D^{-0.53} D \in [1, 192] (R^2 = 0.995)$
25	$I_{1.2} = 24.47D^{-0.60} D \in [1, 171] (R^2 = 0.997)$	$I_{2.2} = 16.92D^{-0.53} D \in [1, 160] (R^2 = 0.998)$
30	$I_{1.2} = 26.24D^{-0.64} D \in [1, 143] (R^2 = 0.996)$	$I_{2.2} = 18.09D^{-0.57} D \in [1, 132] (R^2 = 0.995)$
35	$I_{1.2} = 35.47D^{-0.65} D \in [1, 123] (R^2 = 0.958)$	$I_{2.2} = 19.55D^{-0.58} D \in [1, 112] (R^2 = 0.985)$
40	$I_{1.2} = 40.59D^{-0.78} D \in [1, 103] (R^2 = 0.966)$	$I_{2.2} = 22.15D^{-0.64} D \in [1, 92] (R^2 = 0.984)$
45	$I_{1.2} = 41.12D^{-0.78} D \in [1, 83] (R^2 = 0.932)$	$I_{2.2} = 23.19D^{-0.69} D \in [1, 72] (R^2 = 0.981)$
50	$I_{1.2} = 41.26D^{-0.86} D \in [1, 65] (R^2 = 0.981)$	$I_{2.2} = 23.50D^{-0.74} D \in [1, 55] (R^2 = 0.980)$
55	$I_{1.2} = 38.63D^{-0.88} D \in [1, 53] (R^2 = 0.950)$	$I_{2.2} = 23.31D^{-0.70} D \in [1, 42] (R^2 = 0.932)$
60	$I_{1.2} = 31.49D^{-0.92} D \in [1, 40] (R^2 = 0.992)$	$I_{2.2} = 20.73D^{-0.86} D \in [1, 30] (R^2 = 0.977)$
65	$I_{1.2} = 29.14D^{-0.95} D \in [1, 32] (R^2 = 0.957)$	$I_{2.2} = 18.10D^{-0.91} D \in [1, 22] (R^2 = 0.893)$
70	$I_{1.2} = 23.05D^{-0.96} D \in [1, 25] (R^2 = 0.998)$	$I_{2.2} = 13.04D^{-0.93} D \in [1, 15] (R^2 = 0.995)$
75	$I_{1.2} = 21.13D^{-0.97} D \in [1, 22] (R^2 = 0.994)$	$I_{2.2} = 10.90D^{-0.95} D \in [1, 12] (R^2 = 0.995)$
80	$I_{1.2} = 18.72D^{-0.98} D \in [1, 20] (R^2 = 0.997)$	$I_{2.2} = 9.96D^{-0.95} D \in [1, 11] (R^2 = 0.999)$
85	$I_{1.2} = 18.47D^{-0.99} D \in [1, 18] (R^2 = 0.999)$	$I_{2.2} = 8.17D^{-0.95} D \in [1, 9] (R^2 = 0.999)$

288 Under the condition of AEP < 10 mm, Dens-ID cannot derive the threshold curve
 289 corresponding to even the minimum density value of 1.2 g/cm³, which indicates that the subsequent
 290 rainfall can hardly trigger debris flow JJG. Table 1 also shows that the AEP ranging from 10 to 85
 291 mm can significantly affect the ID threshold curve, because the parameters including α and β
 292 regularly respond to the change in AEP.



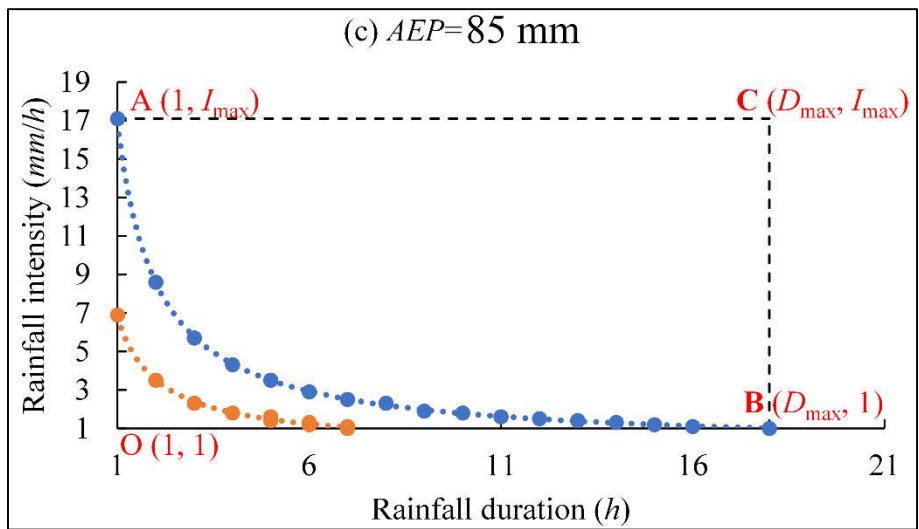
293

294



295

296



297

298 Fig.2 ID threshold curves derived by Dens-ID (the blue dotted line corresponds to 1.2 g/cm^3 , and

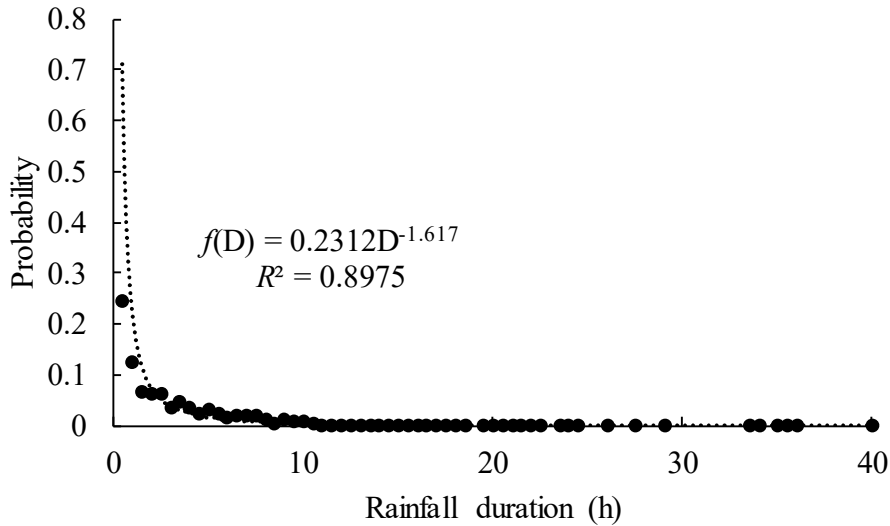
299 the orange dotted line corresponds to 2.2 g/cm^3)

300 There are two ID threshold curves in each subplot of Fig. 2, which correspond to 1.2 g/cm^3 and
301 2.2 g/cm^3 , respectively. Because the debris flow density in JJG varies within a certain range from
302 $1.2\text{--}2.3 \text{ g/cm}^3$, the two ID threshold curves shown in each subplot can be regarded as the upper and
303 lower boundary lines for determining the occurrence of debris flow (Zhang et al., 2020). Within the
304 ID coordinate system, the two derived curves together with the I- and D-axes delineate a closed area
305 shown in Fig.2c. Any subsequence rainfall represented by the combination of I and D falling into
306 W_{ID} may trigger a debris flow. As shown in each subplot, the threshold curve can be represented by
307 the power function $I=\alpha D^\beta$. The variation intervals of the independent (D) and dependent (I) variables
308 of the power function are $[1, D_{\max}]$ and $[1, I_{\max}]$, respectively, where D_{\max} represents the rainfall
309 duration required to trigger debris flow when $I= 1 \text{ mm/h}$, and I_{\max} represents the rainfall intensity
310 required for debris flow formation for $D=1 \text{ h}$. As shown in Fig.2c, independent variable D and
311 dependent variable I can delineate a larger rectangular area (AOBC) in the ID plane than W_{ID} , which
312 is denoted as R_{ID} . The coverage area of R_{ID} is much larger than that of W_{ID} indicating that the
313 proportion of rainfall conditions that can trigger debris flows is low. Therefore, even for AEP=85
314 mm, the occurrence probability of debris flows remains low. As shown in each subplot, each AEP
315 corresponds to a different W_{ID} and R_{ID} , which provides basic data for the quantitative evaluation of
316 the effect of different AEPs on the occurrence probability of debris flows.

317 **4.2 Occurrence probability of debris flow under different AEP**

318 Based on the Monte Carlo method of calculating the definite integral, it is necessary to explore
319 the probability density function of rainfall duration (D) to calculate the occurrence probability of
320 debris flow under different AEP conditions. For the 1094 rainfall events listed in Appendix 1, we

321 found that the probability distribution of rainfall duration D in JJG can be described by a power
 322 function (Fig. 3). As shown in Fig.3, the number of samples with $D < 1$ accounted for 37.7%, $1 < D < 3$
 323 for 23.5%, $3 < D < 5$ for 14.7%, and $5 < D < 10$ for 16.9%; the number of rainfall events with D
 324 exceeding 10 h accounted for only 6.7%.



325

326 Fig. 3 Probability density function of $f(D)$

327 Based on the probability density distribution function $f(D)=0.2312D^{-1.617}$, the cumulative
 328 probability function $cdf(D)$ can be obtained through integration. In $cdf(D)$, denoted as [Eq. Equation](#)
 329 13, the integration constant C needs to be determined.

330
$$cdf(D) = \int_{-\infty}^D f(D) dD = -0.3747 * D^{-0.617} + C \quad (13)$$

331 The range of 0–40 h is evenly divided into 56 statistical intervals (the second column in
 332 Appendix 2, titled “appendix 2-f(D)and CFD(D).xlsx”), and each statistical interval is separated by
 333 0.5 h. The proportion of the sample size in each interval among the 1094 samples can be calculated
 334 and listed in the second column in Appendix 2; the cumulative proportion that increases with D is
 335 also derived and listed in the third column in Appendix 2. The data in the first and third columns of
 336 Appendix 2 are substituted into [Eq. Equation](#) 13 to calculate C . The results show that C increases
 337 with D but gradually stabilizes at approximately 1.04 (the fifth column in Appendix 2). Therefore,

338 C is set to 1.04.

339 Based on the process of calculating P_{df} under different AEP conditions in Section 3.4, the P_{df}
340 corresponding to each AEP in Table 1 is obtained, and the function $P_{df} = f(AEP)$ for describing
341 their relationship has been fitted using the AEP and P_{df} data.

$$\begin{cases} P_{df} = 0 & 0 < AEP < 10 \\ P_{df} = 0.3442e^{0.0457AEP} & 10 \leq AEP \leq 85 \end{cases} \quad (14) P_{df} =$$
$$0.3442e^{0.0457AEP} \quad (14)$$

344 As shown in Eq. Equation 14, the relationship of AEP and P_{df} obeys the rule of exponential
345 function as AEP changes from 10 to 85 mm, whereas $P_{df} = 0$ when AEP is less than 10 mm. The
346 evolution of P_{df} with AEP variation can be divided into two stages (Fig. 4). Two key issues must be
347 stated before discussing the two stages in depth: (1) Based on the calculation results of the Dens-ID
348 model, an upper limit volume of the rainfall-induced solid material supply is derived in JJG, which
349 is the basic condition for determining the scale of debris flow in JJG (Zhang et al., 2020). (2) Based
350 on the principle of water balance, AEP is defined as the rainfall that is preserved in the soil before
351 the triggering rainfall process (Kohler and Linsley, 1951); field observations in JJG show that the
352 AEP is positively correlated with the soil water content (Cui et al., 2007), and the field observations
353 of the Liudaogou catchment in the northern Loess Plateau of China have the same result (Zhu and
354 Shao, 2008); therefore, the AEP is typically used to estimate soil water content (Crozier, 1986; Chen
355 et al., 2018; Zhao et al., 2019b). The water soil content before the triggering rainfall process can be
356 characterized by AEP (Thomas et al., 2019; Schoener and Stone, 2020).

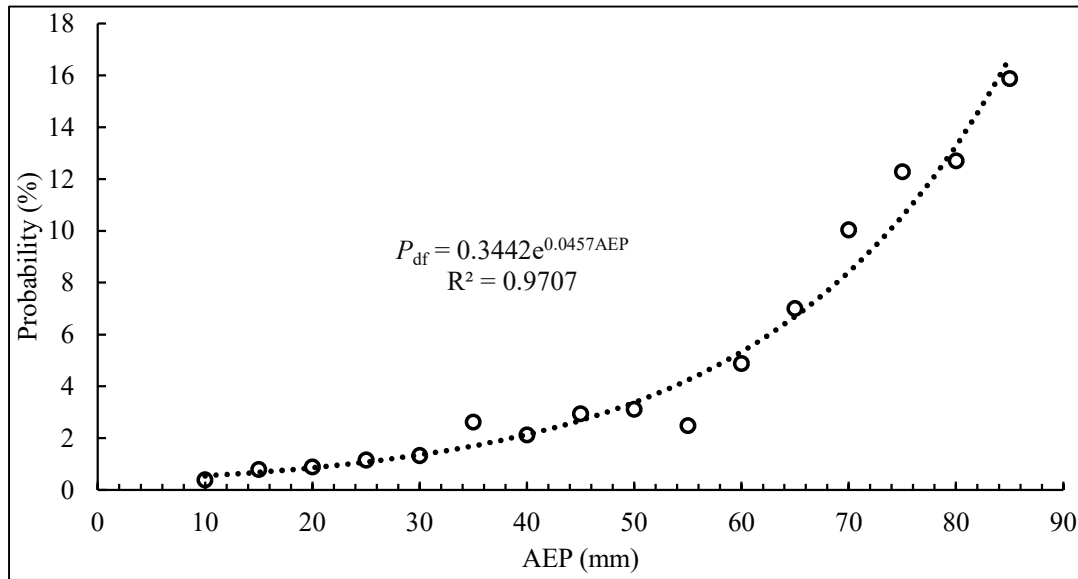


Fig.4 Relationship of P_{df} and AEP derived from Dens-ID

357

358

359

360

361

362

363

364

365

366

367

368

369

370

371

372

Stage 1: The probability of debris flow occurrence in JJG is equal to 0 when the AEP is < 10 mm. Dens-ID estimates the solid material volume by simulating rainfall-induced shallow landslides. According to [Eq. Equation 4](#), the key hydrological process that triggers shallow landslides is the continuous increase in soil water content caused by rainfall infiltration. The increase in soil moisture content reduces soil matrix suction and eventually contributes to shallow landslides. The soil water content of the loose soil mass in JJG is low when the AEP < 10 mm (Long et al., 2020), and a long duration of rainfall infiltration is needed to increase the soil water content. However, based on the infiltration border of Dens-ID ([Eq. Equation 1](#)), limited by the infiltration capacity of the topsoil in JJG, the portion of precipitation that exceeds the infiltration capacity is be converted into runoff; therefore, when the water content of the soil layer in JJG is low, the surface runoff can be rapidly generated. Therefore, the runoff generation rate can be much higher than the supply rate of solid material in the condition of AEP < 10 mm. In this hydrological scenario, Dens-ID determines that even a soil-water mixture with a density of 1.2 g/cm³ is difficult to generate in JJG; thus, the probability of debris flow is 0.

373 Stage 2: When AEP varies within the interval of 10 mm-85mm, the subsequent rainfall is
374 capable of triggering debris flow in JJG. Compared to AEP < 10 mm in Stage 1, the soil water
375 content within JJG increased significantly. Therefore, the solid material from shallow landslides can
376 be immediately ready without a long rainfall infiltration duration, and a large water content of
377 topsoil is beneficial to the rapid generation of runoff (Jones et al., 2017; Hirschberg et al., 2021).
378 When there is a sufficient supply of solid material and runoff, the probability of debris flow
379 occurrence in Stage 2 is significantly increased by the increasing AEP. The relationship between
380 $P_{df} \sim AEP$ can be described by an exponential function of $P_{df} = 0.3442e^{0.0457AEP}$. The exponential
381 function and its boundary show that the increasing tendency of P_{df} is a little sluggish before AEP is
382 equal to 50 mm. The occurrence probability of debris flow in JJG is only 15.88% even when AEP
383 is equal to 85 mm.

384 **5 Discussions**

385 **5.1 Correlation analysis of the two curves derived from Dens-ID and observation data**

386 The AEP in Appendix 1 varied from 0–87.9 mm, according to this range, we can test the
387 reasonability of the relationship between $P_{df} \sim AEP$ shown in Fig. 4. We introduce how to use the
388 rainfall and debris flow data recorded in Appendix 1 to calculate P_{df} : (1) The original AEP value is
389 rounded to one decimal place, and the rounded AEP are listed in the 8th column of Appendix 1,
390 which were sorted from largest to smallest; (2) the maximum AEP_i was set to 85 mm, and [AEP_i,
391 AEP_i-5] was used as the search window to collect the rainfall events and debris flow events; and (3)
392 we count the number of debris flow events N_{df} and the number of rainfall events N_{rain} in each search
393 window and then calculate $P_{df} = N_{df}/N_{rain}$. Based on the above steps, the collected data and calculated

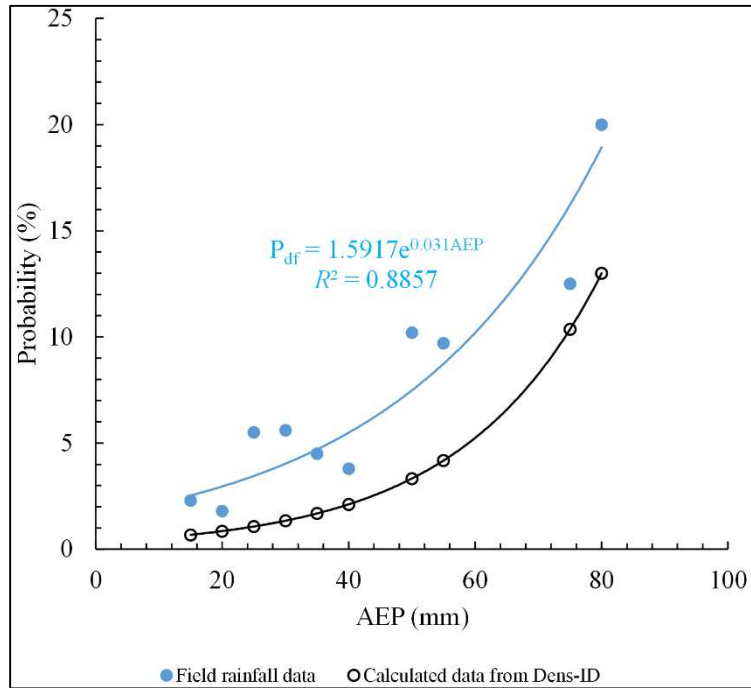
394 P_{df} are listed in Table 2. As shown in Table 2, a positive correlation between the probability of debris
 395 flow occurrence and AEP in JJG was determined. When AEP < 10 mm, a total of 205 rainfall
 396 processes were recorded; however, no debris flow events were observed, and the debris flow
 397 occurrence probability was 0, which is consistent with the results of Stage 1 derived from Dens-ID.

398

Table 2 Collected and calculated P_{df} in each search window

	Field observation data and calculated P_{df}										
AEP	10	15	20	25	30	35	40	45	50	75	80
N_{df}	0	3	2	7	7	4	4	5	3	1	1
N_{rain}	205	133	111	127	124	106	106	49	31	8	5
$P_{df}(\%)$	0	2.3	1.8	5.5	5.6	3.8	3.8	10.2	9.7	12.5	20

399 Based on P_{df} and AEP listed in Table 2, their relationship can be described by the exponential
 400 function denoted as $P_{df} = 1.5917e^{0.031AEP}$, which is similar to [Eq.Equation 14](#) drawn in Fig.4. The
 401 two curves were nearly parallel. [Eq.Equation 12](#) was used to analyze the correlation of the two
 402 curves, and r is equal to 0.93, suggesting they have a very high correlation. Therefore, the function
 403 of $P_{df} = f(AEP)$ derived from Dens-ID, which is used to describe the evolution trend of debris
 404 flow occurrence probability with AEP variation, is reasonable.



405

406

Fig.5 Relationship of AEP and P_{df} obtained from field observation data and Dens-ID model (the blue line is

407

derived from field observation data, and the black line is derived from Dens-ID)

408

We can also see from Fig.5 that although the variation tendencies of the two curves are

409

consistent, a significant bias ~~is~~ existed between them. Basically, the probability value derived from

410

the field observation data is larger than that from the Dens-ID model in the condition of a given

411

AEP. As shown in Fig.5, the blue line fitted through the observation data is above the black line

412

derived from Dens-ID, indicating that Dens-ID underestimated the probability of debris flow

413

occurrence if the observation data were used as the reference. Taking the probability value in the 6th

414

row of Table 2 as references, the error of the [Eq.Equation 14](#) was calculated using the AEP in Table

415

2 as inputs and listed in Table 3.

416

Table 3 Error estimation on the [Eq.Equation 14](#)

AEP	15	20	25	30	35	40	45	50	75	80
Error	0.70	0.53	0.81	0.76	0.63	0.44	0.67	0.57	0.17	0.35

417

It can be seen that very large bias of [Eq.Equation 12](#) is listed in Table 2. However, we cannot

418 conclude that there is a precision problem in the calculation results of the Dens-ID. Because (1)
419 Although 1094 rainfall processes and 37 debris flow events are the field observation data, there are
420 many uncertain factors in [Eq. Equation 7](#) for calculating AEP using these rainfall data (Kim et al.,
421 2021), such as the subjectivity existing in K and n of [Eq. Equation 7](#), which render uncertainty in the
422 calculated AEP. In this case, if the data in Appendix 1 are used as the real value for evaluating the
423 precision of Dens-ID, the error evaluation result may be unfair to Dens-ID. In this case, it is unfair
424 to evaluate the Dens-ID error by using the calculated AEP in Appendix 1 as the true value. However,
425 this uncertainty can show consistent directional deviations because of the fixed values of K and n in
426 [Eq. Equation 7](#); therefore, the uncertainty has no effect on the correlation analysis. (2) To establish
427 the functional relationship between P_{df} -AEP, many rainfall scenarios were simulated using the Dens-
428 ID model. Dens-ID simulated 3376, 3182, 2677, and 2677 rainfall processes with AEP = 20, 40, 45,
429 and 50 mm, respectively. The total number of simulated rainfall processes was significantly larger
430 than that of the 1094 observed rainfall events. The collected 1094 rainfall events still cannot fully
431 reflect all rainfall conditions in nature; that is, the amount of the observed 1094 rainfall data is still
432 inadequate when used as the denominator for calculating the probability of debris flow occurrence
433 in JJG. Therefore, the P_{df} calculated using the field observation data may be generally higher than
434 that calculated using Dens-ID. With the accumulation of rainfall observation data of JJG, it is
435 believed that the Pdf derived from field observation data will gradually decrease until it is close to
436 the calculated value of Dens-ID model. (3) Dens-ID cannot fully and accurately describe the
437 formation process of the debris flow in JJG because of the simplification in theory and boundaries.
438 Dens-ID is also affected by the accuracy of the input parameters (Zhang et al., 2020), which may
439 eventually lead to deviations between the simulation results and field observations.

440 5.2 Potential application and limitation

441 Deriving a quantified functional relationship of P_{df} and AEP would be more conducive to
442 examining the correspondence between these two parameters. Using mathematical physics method,
443 the function of $P_{df} = f(AEP)$ was firstly derived which can help us to learn more from the derived
444 $P_{df} = f(AEP)$.

445 Firstly, AEP is indeed an important factor affecting debris flow. Generally, there is the
446 following consensus in the field of debris flow: the greater the AEP, the higher the probability (P_{df})
447 of subsequent rainfall triggering the debris flow (De Vita et al., 2000; Bel et al., 2017). However,
448 this fuzzy qualitative description cannot explain the influence degree of AEP on the probability of
449 debris flow induced by subsequent rainfall. It can be seen from $P_{df} = f(AEP)$ that there are two
450 key value nodes of AEP affecting P_{df} : (1) point 10 mm: the case of $AEP < 10$ mm indicates that
451 any subsequent rainfall cannot trigger debris flow in JJG. Because the supply rate of solid material
452 is much lower than the runoff generation rate during subsequent rainfall in JJG, the water-soil
453 mixture within tends to be a hyperconcentrated flow rather than a debris flow (Long et al., 2020);
454 (2) Point 50 mm: the case of $10 \text{ mm} \leq AEP \leq 50 \text{ mm}$ means that the soil water content increases
455 significantly compared to $AEP < 10$ mm, but a necessary infiltration time to increase it to the critical
456 state for triggering shallow landslides is still required. Therefore, limited by the supply rate of the
457 solid material, the increasing rate of P_{df} is sluggish. The case of $50 \text{ mm} < AEP \leq 85 \text{ mm}$ represents
458 the soil water content is relatively larger, the solid material from shallow landslides can be
459 immediately ready without a long rainfall infiltration duration, and a large soil water content of
460 topsoil is beneficial to the rapid generation of runoff (Jones et al., 2017; Hirschberg et al., 2021).
461 When there is a sufficient supply of provenance and runoff, the probability of debris flow occurrence

462 in this subprocess is significantly enhanced by the increasing AEP.

463 Secondly, Rainfall-induced debris flow is a small probability event compared with the rainfall
464 frequency in nature. JJG is well-known due to its high-frequency debris flow event. However, the
465 formation probability of debris flow in JJG induced by subsequence rainfall is only 15.88% even
466 the AEP reaches to 85 mm. Therefore, debris flow induced by rainfall in JJG is a small probability
467 event compared with the rainfall frequency. The figure of 15.88% means that the efficiency of rain-
468 induced debris flow is extremely low, which also indicates that the formation of debris flow is an
469 extremely complex physical process, in which rainfall is only one of the motivating factors, and
470 there are other more important internal factors affecting the formation of debris flow, such as
471 topography, source recharge and fluid characteristics of debris flow (Zhang et al., 2020). Thirdly, in
472 practical application, when the AEP in JJG is calculated according to [Eq. Equation 7](#), the derived
473 exponential function can help us to assess the probability of debris flow in JJG triggered by
474 subsequent rainfall, according to which debris flow warning information can be issued in advance
475 to provide technical support for disaster prevention and reduction.

476 Our study also has its own limitations and needs to be listed for providing directions for
477 subsequent investigation. (1) Long-term observation data should be used to deduce the functions of
478 $P_{df} = f(AEP)$, however, the number of debris flow gullies with long-term observational data
479 worldwide is less than 10 (Hürlimann et al., 2019), accordingly, the function of $P_{df} = f(AEP)$
480 cannot yet be derived in other debris-flow gullies. (2) Dens-ID model assumes that the solid
481 material mainly comes from shallow landslides. However, the formation mechanism and solid
482 source supply mode of runoff-induced debris flow are different. Therefore, the functional of $P_{df} =$
483 $f(AEP)$ for runoff-induced debris flow still needs to be studied with the help of other physical

484 models. (3) The calculation result of $P_{df} = f(AEP)$ derived from Dens-ID model has a large bias
485 from the observation data, the authors think that the main reason is insufficient field observation
486 data especially inadequate rainfall data. Basically, even for high-frequency debris flow gullies like
487 JJG, the success rate of debris flow induced by rainfall is still very low. Continuous increase of
488 rainfall and debris flow observation data will make the growth rate of N_{rain} in Table 2 much higher
489 than that of N_{df} . Therefore, with the accumulation of rainfall observation data of JJG, it is believed
490 that the P_{df} derived from field observation data will gradually decrease until it is close to the
491 calculated result of Dens-ID model. Therefore, the authors will continue to collect field observation
492 data of JJG in the later period, and constantly verify the accuracy of [Eq. Equation 14](#) derived from
493 Dens-ID.

494 **5 Conclusions**

495 The Dens-ID model and Monte Carlo integral equation is used to derive function of $P_{df} =$
496 $f(AEP)$. The functional relationship is verified using a large amount of field observation data from
497 JJG. The following conclusions are drawn as follows.

498 The positive relationship between P_{df} and AEP is now described by a clear mathematical
499 equation in this study. the effective range of AEP that can affect debris flow formation verifies within
500 10–85 mm. Based on the simulation results, the probability of debris flow occurrence in JJG is 0 in
501 the condition of $AEP < 10$ mm, and the relationship between P_{df} and AEP can be described by an
502 exponential function when $10 \text{ mm} \leq AEP \leq 85 \text{ mm}$. The plausibility of the first two evolution stages
503 of the P_{df} -AEP piecewise function is effectively confirmed by the field observation data because the
504 P_{df} -AEP relationship obtained from field observation data is highly correlated with the simulation
505 results of Dens-ID. However, the reasonability of the last two stages of the P_{df} -AEP piecewise

506 function cannot be tested because of the lack of field observation data, and the errors of the P_{df} -AEP
507 piecewise function cannot be verified because of the uncertainty of the AEP derived from the
508 observation rainfall data.

509 This study mathematically confirms that "the greater the AEP, the higher the probability of
510 subsequent rainfall triggering debris flow" and quantifies this qualitative conclusion using piecewise
511 functions. This can effectively reveal the essential relationship between the two natural events of
512 rainfall and debris flow, quantitatively describe the impact of different AEPs on the probability of
513 debris flow occurrence, and provide key technical support for the early warning of debris flows.

514 **Acknowledgement:**

515 This work was supported by the National Key Research and Development Program of China
516 (2023YFC3007205), the West Light Foundation of The Chinese Academy of Science, National
517 Natural Science Foundation of China (No. 42271013, No. 42001100), Project of the Department of
518 Science and Technology of Sichuan Province (No. 2023ZHCG0012).

519 **References**

520 Abraham, M.T., Satyan, N., Rosi, A., Pradhan, B., Segoni, S.: Usage of antecedent soil moisture for
521 improving the performance of rainfall thresholds for landslide early warning. *Catena*, 200,
522 105147, 2021.

523 Abraham, M.T., Satyam, N., Pradhan, B., Alamri, A.M.: Forecasting of landslides using rainfall
524 severity and soil wetness: A probabilistic approach for Darjeeling Himalayas. *Water* (Switzerland)
525 12, 1–19, 2020.

526 Adams, B., Fraser, H., Howard, C., Hanafy, M.: Meteorological data analysis for drainage system
527 design. *J. Environ. Eng.* 112, 1986.

528 Albert, G.E.: A general theory of stochastic estimates of the Neumann series for solution of certain
529 Fredholm integral equations and related series, in: M.A. Meyer (Ed.), Symposium of Monte Carlo
530 Methods, Wiley, New York, 1956.

531 Bel, C., Liébault, F., Navratil O., Eckert N., Bellot H., Fontaine, F., Laigle, D.: Rainfall control of
532 debris-flow triggering in the Réal Torrent, Southern French Prealps, 291, 17-32, 2017.

533 Bennett, G.L., Molnar, P., Mcardell, B.W., Burlando, P.: A probabilistic sediment cascade model of
534 sediment transfer in the Illgraben. *Water Resources Research*, 50, 1225-1244, 2014.

535 Bernard, M., Gregorette, C.: The use of rain gauge measurements and radar data for the model-based
536 prediction of runoff-generated debris flow occurrence in early warning systems. *Water Resources*
537 *Research*, 57, e2020WR027893, 2021.

538 Berti, M., Simoni, A.: Experimental evidences and numerical modelling of debris flow initiated by
539 channel runoff. *Landslides*, 3, 171-182, 2005.

540 Calvo, B., Savi, F.: A real-world application of Monte Carlo procedure for debris flow risk
541 assessment, *Computers and Geosciences*, 35(5), 967-977, 2009.

542 Castillo, V.M., Gómez-Plaza, A., Martínez-Mena, M.: The role of antecedent soil water content in
543 the runoff response of semiarid catchments: a simulation approach. *Journal of Hydrology*, 284,
544 114-130, 2003.

545 Chen, C.W., Oguchi, T., Chen, H., Lin, G.W. Estimation of the antecedent rainfall period for mass
546 movements in Taiwan, *Environmental Earth Sciences*, 77, 184, 2018.

547 Chen, C.W., Saito, H., Oguchi, T.: Analyzing rainfall-induced mass movements in Taiwan using the
548 soil water index, *Landslides*, 14, 1031-1041, 2017.

549 Coe, J.A., Kinner, D.A., Godt, J.W. Initiation conditions for debris flows generated by runoff at

550 Chalk Cliffs, central Colorado. *Geomorphology*, 3, 270-297, 2008.

551 Crozier, M.J.: *Landslides: causes, consequences & environment*. Croom Helm, London, p 25, 1986.

552 Cui, P., Zhu, Y.Y., Chen, J., Han, Y.S., Liu, H.J.: Relationships between antecedent rainfall and
553 debris flows in Jiangjia Ravine, China. In: Chen & Major, eds., *Debris-Flow Hazards Mitigation:
554 Mechanics, Prediction, and Assessment*, Millpress, Netherlands, 3-10, 2007.

555 De Vita, P.: Fenomeni d'instabilita' delle coperture piroclastiche dei Monti Lattari, di Sarno e di
556 Salerno (Campania) ed analisi degli eventi pluviometrici determinanti. *Quad. Geol. Appl.*, 7, 213–
557 239, 2000.

558 Donovan, I.P., Santi, P.M. A probabilistic approach to post-wildfire debris-flow volume modeling,
559 *Landslides*, 14(4): 1345-1360, 2017.

560 Fiorillo, F., Wilson, R.C. Rainfall induced debris flows in pyroclastic deposits, Campania (southern
561 Italy). *Engineering Geology*, 75, 263-289, 2004.

562 Gabet, E.J., Mudd, S.M.: The mobilization of debris flows from shallow landslides. *Geomorphology*
563 1, 207-218, 2006.

564 Han, Z., Chen, G.Q., Li, Y.G., He, Y.: Assessing entrainment of bed material in a debris-flow event:
565 a theoretical approach incorporating Monte Carlo method: *Assessing Entrainment of Bed
566 Material by Debris Flow, Earth surface processes and landforms*, 40(14): 1877-1890, 2015.

567 Hirschberg, J., Badoux, A., McArdell, B.W., Leonarduzzi, E., Molnar, P.: Evaluating methods for
568 debris-flow prediction based on rainfall in an Alpine catchment. *Nat. Hazards Earth Syst. Sci.*,
569 21, 2773-2789, 2021.

570 Hong, M., Kim, J., Jeong, S.: Rainfall intensity-duration thresholds for landslide prediction in South
571 Korea by considering the effects of antecedent rainfall. *Landslides*, 15, 523–534, 2018.

572 Hu, W., Xu, Q., Wang, G.H., van Asch, T.W.J., Hicher, P.Y.: Sensitivity of the initiation of debris
573 flow to initial soil moisture. *Landslides* 12, 1139–1145, 2015.

574 Huang, C.H.: Critical rainfall for typhoon-induced debris flows in the Western Foothills, Taiwan.
575 *Geomorphology*, 185, 87-95, 2013.

576 Hürlimann, M. Coviello, V., Bel, C., Guo, X.J., Berti, M., Graf, C., Hübl, J., Miyata, S., Smith, J.B.,
577 Yin, H.Y.: Debris-flow monitoring and warning, Review and examples. *Earth-Science Reviews*,
578 199, 102981, 2019.

579 Iverson, R. M., Reid, M. E., LaHusen, R. G.: Debris Flow Mobilization from Landslides. *Annu. Rev.*
580 *Earth Planet*, 25: 85-138, 1997.

581 Jones, R., Thomas, R.E., Peakall, J., Manville, V.: Rainfall-runoff properties of tephra: Simulated
582 effects of grain-size and antecedent rainfall. *Geomorphology*, 282, 39-51, 2017.

583 Kim, S.W., Chun, K.W., Kim, M., Catani, F., Choi, B., Seo, J.: Effect of antecedent rainfall
584 conditions and their variations on shallow landslide-triggering rainfall thresholds in South Korea.
585 *Landslides*, 18, 569-582, 2021.

586 Kohler, M.A., Linsley, R.K.: Predicting the runoff from Storm Rainfall. US Department of
587 Commerce, Weather Bureau, Washington, D.C, 1951.

588 Le Bissonnais, Y., Renaux, B., Delouche, H. Interactions between soil properties and moisture
589 content in crust formation, runoff and interrill erosion from tilled loess soils. *Catena*, 25(1), 33-
590 46, 1995.

591 Li, L., Zhang, S.X., Li, S.H., Qiang, Y., Zheng, Z., Zhao, D.S.: Debris Flow Risk Assessment
592 Method Based on Combination Weight of Probability Analysis, *Advances in civil engineering*,
593 2021, 1-12, 2021.

594 Liu, D.L., Zhang, S.J., Yang, H.J., Zhao, L.Q., Jiang, Y.H., Tang, D., Leng, X.P.: Application and
595 analysis of debris-flow early warning system in Wenchuan earthquake-affected area. *Nat. Hazards*
596 *Earth Syst. Sci.*, 16, 483-496, 2016.

597 Liu, X.L., Wang, F., Nawnit, K., Lv, X.F., Wang, S.J. Experimental study on debris flow initiation.
598 *Bulletin of Engineering Geology and the Environment*, 79, 1565-1580, 2020.

599 Long, K., Zhang, S.J., Wei, F.Q., Hu, K.H., Zhang, Q., Luo, Y. A hydrology-process based method
600 for correlating debris flow density to rainfall parameter and its application on debris flow
601 prediction. *Journal of Hydrology*, 589, 125124, 2020.

602 Luk, S.H.: Effect of antecedent soil moisture content on rainwash erosion. *Catena*, 12, 129-139,
603 1985.

604 Marra, F., Destro, E., Nikolopoulos, E.I., Zocatelli, D., Creutin, J.D., Guzzetti, F., Borga, M.:
605 Impact of rainfall spatial aggregation on the identification of debris flow occurrence thresholds.
606 *Hydrol. Earth Syst. Sci.*, 21, 4525-4532, 2017.

607 Paola, F.De., Risi, R.De., Crescenzo, G. Di, Giugni, M., Santo, A., Speranza, G.: Probabilistic
608 Assessment of Debris Flow Peak Discharge by Monte Carlo Simulation, *Journal of Risk and*
609 *Uncertainty in Engineering Systems, Part A: Civil Engineering*, 3(1), A4015002, 2017.

610 Papa, M.N., Medina, V., Ciervo, F., Bateman, A.: Derivation of critical rainfall thresholds for
611 shallow landslides as a tool for debris flow early warning systems. *Hydrol. Earth Syst. Sci.* 17,
612 4095-4107, 2013.

613 Peres, D.J., Cancelliere, A.: Derivation and evaluation of landslide-triggering thresholds by a Monte
614 Carlo approach. *Hydrol. Earth Syst. Sci.*, 18, 4913-4931, 2014.

615 Peres, D.J., Cancelliere, A.: Modeling impacts of climate change on return period of landslide

616 triggering. *Journal of Hydrology*, 567, 420-434, 2018.

617 Richards, L.A. Capillary condition of liquids in porous mediums. *Physics* 1, 318–333, 1931.

618 Schoener, G., Stone, M.C.: Monitoring soil moisture at the catchment scale-A novel approach
619 combining antecedent precipitation index and rader-derived rainfall data, *Journal of Hydrology*,
620 589, 125155, 2020.

621 Segoni, S., Piciullo, L., Gariano, S.L.: A review of the recent literature on rainfall thresholds for
622 landslide occurrence, *Landslides*, 15:1483-1501, 2018b.

623 Segoni, S., Rosi, A., Lagomarsino, D., Fanti, R., Casagli, N.: Brief communication: Using averaged
624 soil moisture estimates to improve the performances of a regionalscale landslide early warning
625 system. *Nat. Hazards Earth Syst. Sci.* 18, 807–812, 2018a.

626 Senthilkumar, V., Chandrasekaran, S.S., Maji, V.B.: Geotechnical characterization and analysis of
627 rainfall-induced 2009 landslide at Marappalam area of Nilgiris district, Tamil Nadu state, India.
628 *Landslides*, 14, 1803-1814, 2017.

629 Tang, H., Mcguire, L.A., Kean, J.W., Smith, J.B.: The impact of sediment supply on the initiation
630 and magnitude of runoff-generated debris flows. *Geophysical Research Letters*, 47,
631 e2020GL087643, 2020.

632 Thomas, M.A., Collins, B.D., Mirus, B.B.: Assessing the feasibility of satellite-based thresholds for
633 hydrologically driven landsliding. *Water Resource Research*, 55, 9006-9023, 2019.

634 Tisdall, A.: Antecedent soil moisture and its relation to infiltration. *Aust. J. Agric. Res.*, 2 (3), 342–
635 348, 1951.

636 Van Genuchten, M.: A closed form equation for predicting the hydraulic conductivity of unsaturated
637 soils. *Soil Sci. Soc. Am. J.* 44, 892–898, 1980.

638 Wei, F.Q., Hu, K.H., Zhang, J., Jiang, Y.H., Chen, J.: Determination of effective antecedent rainfall
639 for debris flow forecast based on soil moisture content observation in Jiangjia Gully, China. In:
640 DeWrachien, D., Brebbia, C.A., Lenzi, M.A., eds., *Monitoring, Simulation, Prevention and*
641 *Remediation of dense debris flows II*. WIT Transactions on Engineering Sciences, England. 13-
642 22, 2008.

643 Yan, Z.Z., Hong, Z.M.: Using the Monte Carlo method to solve integral equations using a modified
644 control variate. *Applied mathematics and computation*, 242,764-777, 2014.

645 Yang, H.J., Zhang, S.J., Hu, K.H., Wei, F.Q., Wang, K., Liu S.: Field observation of debris flow
646 activities in the initiation area of Jiangjia Gully, Yunnan Province, China, *Journal of Mountain*
647 *Science*, 19(6): 1602-1617, 2022.

648 Zeng, Q.L., Yue, Z.Q., Yang, Z.F., Zhang, X.J.: A case study of long-term field performance of
649 check-dams in mitigation of soil erosion in Jiangjia stream, China. *Environ Geol* 58:897–911,
650 2009.

651 Zhang, S.J., Xu, C.X., Wei, F.Q., Hu, K.H., Xu, H., Zhao, L.Q., Zhang, G.P.: A physics-based model
652 to derive rainfall intensity-duration threshold for debris flow. *Geomorphology*, 351, 106930, 2020.

653 Zhang, S.J., Yang, H.J., Wei, F.Q., Jiang, Y.H., Liu, D.L.: A model of debris flow forecast based on
654 the water-soil coupling mechanism. *Journal of Mountain Science*, 25, 757-763, 2014.

655 Zhang, S.J., Xia, M.Y., Li, L., Yang, H.J., Liu, D.L., Wei, F.Q.: Quantify the effect of antecedent
656 effective precipitation on rainfall intensity-duration threshold of debris flow. *Landslides*, 20,
657 1719-1730, 2023.

658 Zhao, B.R., Dai, Q., Han, D.W., Dai, H.C., Mao, J.Q., Zhuo, L.: Probabilistic thresholds for
659 landslides warning by integrating soil moisture conditions with rainfall thresholds. *Journal of*

660 Hydrology, 574, 276-287, 2019a.

661 Zhao, B.R., Dai, Q., Han, D., Dai, H., Mao, J., Zhuo, L., Rong, G.: Estimation of soil moisture using
662 modified antecedent precipitation index with application in landslide predictions. Landslides 16,
663 2381–2393, 2019b.

664 Zhu, Y.J., Shao, M.G.: Variability and pattern of surface moisture on a small-scale hillslope in
665 Liudaogou catchment on the northern Loess Plateau of China, Geoderma, 147, 185-191, 2008.

666 Zhuang, J.Q., Cui, P., Wang, G.H., Chen, X.Q., Iqbal, J., Guo, X.J.: Rainfall thresholds for the
667 occurrence of debris flows in Jiangjia Gully, Yunnan Province, China. Eng. Geol. 195, 335–346,
668 2015.